

An Unprecedented Chalcogenide-cluster-based Semiconducting Nanotube Array with Oriented Photoconductive Behavior

Jiaqi Tang

Soochow University

Xiang Wang

Soochow University <https://orcid.org/0000-0001-7354-6491>

Jiaxu Zhang

Soochow University

Jing Wang

Soochow University

Wan-Jian Yin

Soochow University <https://orcid.org/0000-0003-0932-2789>

Dongsheng Li

China Three Gorges University

Tao Wu (✉ wutao@suda.edu.cn)

Soochow University <https://orcid.org/0000-0003-4443-1227>

Article

Keywords: carbon nanotubes (CNTs), chalcogenides

Posted Date: February 5th, 2021

DOI: <https://doi.org/10.21203/rs.3.rs-151827/v1>

License: © ⓘ This work is licensed under a Creative Commons Attribution 4.0 International License.

[Read Full License](#)

Version of Record: A version of this preprint was published at Nature Communications on July 13th, 2021. See the published version at <https://doi.org/10.1038/s41467-021-24510-0>.

Abstract

The interesting physical and chemical properties of carbon nanotubes (CNTs) have prompted the search for diverse inorganic nanotubes with different compositions to expand the number of available nanotechnology applications. Among these materials, novel crystalline inorganic nanotubes with well-defined structures and uniform sizes are extremely suitable for understanding structure–activity relationships. However, their preparation comes with large synthetic challenges owing to their inherent complexity. Herein, we report the first example of a crystalline nanotube array based on a supertetrahedral chalcogenide cluster, $K_3[K(Cu_2Ge_3Se_9)(H_2O)]$ (**1**). To the best of our knowledge, this nanotube array possesses the largest diameter of crystalline inorganic nanotubes reported to date and exhibits an excellent structure-dependent electric conductivity and an oriented photoconductive behavior. This work represents a significant breakthrough both in terms of the structure of cluster-based metal chalcogenides and in the conductivity of crystalline nanotube arrays (i.e. an enhancement of ~ 4 orders of magnitude).

Introduction

Over the past three decades, one-dimensional (1D) hollow tubular nanomaterials have long been the focus of considerable interest in the physics, chemistry, and materials communities because of their unique physical and chemical properties, as well as their diverse potential applications since the discovery of carbon nanotubes (CNTs) by Iijima in 1991.^{1–8} To date, several multifarious nanotubular architectures with pure inorganic or inorganic–organic hybrid or pure organic components as the nanotube skeleton have been synthesized and applied in various fields, such as catalysis,^{9,10} molecular capillaries,¹¹ energy storage,^{12,13} and biological models.^{14,15} Among the various nanotubular materials, robust inorganic nanotubes with high thermal and chemical stabilities are considered extremely promising for a wide range of interesting potential properties and applications, and therefore, these materials have attracted a great deal of scientific attention.^{2,7}

Scheme 1. Comparisons of **a** traditional nanotubes and **b** a crystalline nanotube array. Comparison of **c** an atomic-layered nanotube and **d** a cluster-based nanotube. (see Supplementary Files)

Generally, inorganic nanotubes are formed by rolling up exfoliated two-dimensional (2D) flat sheets of corresponding lamellar materials under special non-equilibrium conditions (chemical vapor deposition, flash evaporation and discharge evaporation)^{16,17} or constructed through a bottom-up approach from basic inorganic elements.^{6,7,16–25} The nanotubes fabricated via the rolling-up approach are usually in the form of fully or partially disordered arrays with large size distributions (**Scheme 1a**), which may require additional purification steps to avoid affecting their applications.^{6,7,19} In contrast, high-quality nanotubes, synthesized using a bottom-up strategy and possessing an atomically precise structure and uniform size, are highly desirable for understanding structure-property relationships and future applications.^{7,20} Moreover, this type of nanotube is often negatively charged and can be assembled into crystal arrays by ionic or other weak interactions (**Scheme 1b**), thereby providing a platform for studying

ion transportation and ionic conduction within or outside the nanotubes;^{6, 7, 17} this is important in the context of nanoelectronics and biotechnology.²⁶ However, only a small number of well-defined crystalline inorganic nanotube arrays have been reported owing to synthetic challenges, such as a poor design due to the inherent complexities of synthetic processes for pure inorganic materials,¹⁶ thereby contrasting with the case of rich inorganic-organic hybrid tubular structures (*e.g.*, metal–organic nanotubes).^{3, 4, 11, 26} In addition, the majority of crystalline inorganic nanotube arrays have been constructed using metal oxides, such as **PTC-118** ($\{(EMIm)_3[(H_2O) \subset Ti_6O_6(\mu_2-OH)_3(SO_4)_6]\}_n$), as recently reported by Zhang *et al.*⁷ To date, a limited number of chalcogenide-based crystalline tubular compounds have been documented, and their photo-/electroconductivity properties remain unexplored;^{16, 17, 20} however, they are particularly desirable for applications in nanoelectronics and optoelectronics as semiconducting chalcogenides could be advantageous in opto-/electronic property compared with insulating oxides thanks to the lower electronegativities of S/Se/Te compared to that of O.²⁷ The development of new chalcogenide-based crystalline nanotube arrays and subsequent study of their potential photo-/electroconductivity properties and corresponding structure-activity relationships for high-performance photoelectric conversion devices are therefore of particular interest. In addition, compared with atomic-layered single-wall nanotubes (**Scheme 1c**), the crystalline inorganic nanotube arrays assembled by clusters could possess greater numbers of exposed sites or external surfaces due to the significantly more rugged surface constructed by protruding clusters (**Scheme 1d**); this could also result in interesting new properties.

Thus, we herein report the preparation of a novel supertetrahedral chalcogenide-cluster-based compound $\{K_3[K(Cu_2Ge_3Se_9)(H_2O)]\}$ (**1**), featuring an unprecedented 1D nanotubular structure, and examination of its oriented photoconductive property. We expect that this structure will be distinct from the traditional 0D discrete clusters, 1D chains, 2D layers and 3D frameworks constructed by supertetrahedral chalcogenide clusters during the past 50 years,²⁸⁻³⁰ and that it will constitute the first significant breakthrough since the emergence of the supertetrahedral $Na_4Ge_4S_{10}$ T2 cluster (“T” denotes tetrahedral, 2 denotes the number of Ge sites along the tetrahedron edge) in 1971.³¹

Results And Discussion

Crystal structure. Red rod crystals of **1** (**Supplementary Fig. 1**) were synthesized *via* the solvothermal method (see the Experimental section in the Supporting Information for details). Single-crystal X-ray diffraction (SCXRD) analysis revealed that **1** crystallized in a highly symmetrical trigonal system with an *R*-3 space group (**Supplementary Table 1**), and exhibited a unique nanotubular structure (Fig. 1). The asymmetric unit of **1** contains 19 crystallographically independent sites, comprising two Cu, three Ge, and nine Se, in addition one water guest molecule, four potassium counter-cations (**Supplementary Fig. 2**). In addition, the valence state of Cu was confirmed to be monovalent by X-ray photoelectron spectroscopy (XPS) (**Supplementary Fig. 3**), while the phase purity was verified using powder X-ray diffraction (PXRD) (**Supplementary Fig. 4**). Through combination of the results of SCXRD, energy-dispersive spectroscopy

(**Supplementary Fig. 5**), thermogravimetric analysis (TGA) (**Supplementary Fig. 6**) and elemental analysis, the empirical formula of **1** was determined to be $\text{K}_4\text{Cu}_2\text{Ge}_3\text{Se}_9(\text{H}_2\text{O})$.

As shown in Fig. 1, the primary building unit (PBU) of **1** is a heterometallic supertetrahedral T2-CuGeSe cluster, which can be viewed as a homometallic supertetrahedral T2-GeSe cluster with one of the four corner germanium sites occupied by copper (Cu(1) in **Supplementary Fig. 2**). The $[\text{Cu}(1)\text{Se}_4]$ tetrahedron unit is slightly distorted in comparison with the $[\text{GeSe}_4]$ tetrahedron unit in the homometallic supertetrahedral T2-GeSe cluster (Fig. 1a and 1b), likely due to the mismatch of the local charge caused by the lower valence state of Cu compared with that of Ge. In the traditional view, these six staggered PBUs are connected end-to-end by six Cu ions to form a novel giant hexagonal wheel-shaped cluster ($[\text{Cu}_6(\text{CuGe}_3\text{Se}_{10})_6]$) with the C_{3i} point group (Fig. 1c and **Supplementary Fig. 7**), which can serve as the secondary building units (SBUs) for further assembly. More specifically, in this wheel-shaped cluster, each single independent Cu(2) atom is located close to the Cu(1) site and interlinked two adjacent T2-CuGeSe clusters *via* three Cu-Se bonds (Fig. 1c). Among the three Cu-Se bonds, two originate from the bonding of the Cu(2) atom with two edge Se atoms next to the Cu(1) site of one T2 cluster, while the remaining Cu-Se bond comes from the bonding of the Cu(2) atom with the corner $\text{Se}(4)^{2-}$ of the other T2 cluster. Furthermore, the three Cu-Se bonds are coplanar with unequal length, and the corresponding Se-Cu-Se bond angles are also diverse from one another (**Supplementary Fig. 8**). It should be noted that the planar trigonal coordination mode of Cu between two supertetrahedral clusters is rare,³² in contrast to the single linearly-coordinated Cu^+ species between clusters³³⁻³⁵ and the tetrahedrally-coordinated Cu^+ residing in the cluster. According to Pauling's electrostatic valence rule, the theoretical residual charges of the Se^{2-} ions coordinated with the Cu^+ ions in an isolated T2-CuGeSe cluster, all increased by -0.75, when replacing one Ge^{4+} cation from an isolated T2-GeSe cluster with one low-valent Cu^+ cation (Fig. 1a and 1b), thereby resulting in a serious mismatch of local charge. To address this issue, a single low-valent Cu^+ cation was introduced and triangularly coordinated with three Se^{2-} ions between two T2 clusters to maximally balance the excess local negative charge. Meanwhile, accompanying the looser geometrical demand of selenide compared to sulfide, an exceptional heterometallic supertetrahedral T2 cluster-based wheel-shaped ring was formed, which contrast to the 3D frameworks constructed by homometallic T2-GeS sulfide clusters with linearly-, trigonally- or tetrahedrally-coordinated low-valent transition metal ions (such as Cu^+ , Ag^+ , and Mn^{2+}).³²⁻³⁷ To further lessen the excess high negative charge at the terminal Se site that is linked with the Cu(1), and facilitate the global charge balance, these large wheels are connected end-to-end through sharing of the terminal Se^{2-} ion close to the Cu(1) site with the $\text{Ge}(3)^{4+}$ of the other T2 cluster, ultimately forming an unprecedented supertetrahedral chalcogenide-cluster-based infinite nanotube ($[\text{Cu}_6(\text{CuGe}_3\text{Se}_{10})_6]_n$) along the *c* direction, with an outer diameter of 25.97 Å and an inner opening window of 12.91×19.86 Å (Fig. 1c and 1d). To the best of our knowledge, this structure represents the largest example of a crystalline inorganic nanotube to date (**Supplementary Table 2**). Moreover, the wall of the nanotube was composed of 16-membered ring (16 MR) windows formed by four T2-CuGeSe clusters with pore sizes of 3.59×6.47 Å (**Supplementary Fig. 9**). Because **1** cannot be dispersed in common solvents, an ultrathin section sample of **1** was observed by high resolution

transmission electron microscopy (HRETM) (**Supplementary Fig. 10**), revealing the high crystallinity of **1** with distinct interplanar lattice fringes of 0.78 nm, which is consistent with the observation of an XRD peak at $2\theta = 11.7^\circ$ (**Supplementary Fig. 4**).

Furthermore, the negative charges on the skeleton of the nanotube are balanced by pure K^+ ions located at the gaps between the nanotubes and by hydrated K^+ ions filling in the channel. These K^+ ions, along with guest water molecules residing inside and outside of the nanotube, play a key role in constructing and stabilizing the Nanotubes, and promote their further packing into a highly ordered honeycomb-like hexagonal symmetrical array (Fig. 1e) *via* complex weak interactions such as hydrogen bonding and electrostatic interactions (**Supplementary Fig. 11**).^{6,7,20} Thus, control experiments demonstrated that K_2S is indispensable for the formation of **1**. Figure 1f also displays the pillared stacking of the wheel clusters in the axial direction and the assembly of nanotubes to form a 1D tubular superlattice. The nanotube can also be viewed in a different way, where six 1D chains, formed by the end-to-end linkage of T2-CuGeSe clusters through sharing corner Se^{2-} ions coordinated with Cu(1) and Ge(3) atoms, bind alternately with six Cu^+ ions in the same manner as above to form nanotubes (Fig. 1c, 1g, and **Supplementary Fig. 12**). This assembly mode is supported by the observation of **2**, a 1D chain structure based on T2-CdGeSe clusters (**Supplementary Fig. 13**), which forms upon replacing the copper salt with a cadmium salt during preparation. Compound **2** was comprehensively characterized (**Supplementary Fig. 14–18 and Supplementary Table 3**), and upon comparison with the structure of **1**, Cd^{2+} was found to occupy the Cu^+ site of the T2-CuGeSe cluster in **2**, resulting in decreased theoretical residual charges from the surrounding Se atoms, which correspondingly reduces the further bonding capability of the Se^{2-} ions on the edges of the cluster toward other metal ions, thereby leading to the formation of 1D chains rather than 1D tubules. We therefor speculated that the dissimilar ionic radii and coordination modes between Cd^{2+} and Cu^+ may also contribute to such difference.

Electrical conductivity measurement. The optical indirect bandgap of **1** was calculated to be 1.03 eV from the transformed solid-state UV-Vis diffuse reflectance spectrum (**Supplementary Fig. 19**). This value was considered relatively narrow and largely red shifted by 0.63 eV compared with the corresponding value of **2** (i.e., 1.66 eV), thereby indicating the superior conductivity of **1**.³⁸ This was confirmed by electrical conductivity measurements on a single crystal of **1** through a direct-current two-terminal method (Fig. 2a and 2b).

As shown in Fig. 2c, the electric conductivity of **1** was determined to be $7.6 \times 10^{-6} \text{ S cm}^{-1}$ at 40°C along the *c* axis, and was positively related to temperature, exhibiting typical semiconductive characteristics. The corresponding activation energy (E_a) was calculated to be 0.52 eV (Fig. 2d). The electrical conductivity of **1** was found to be approximately 10000-times higher than those of other crystalline nanotube arrays, and among one of the highest values for crystalline semiconductor materials containing copper or/and chalcogenide elements (**Supplementary Table 4**).^{6,7,39–42} Moreover, the photoconductivity of **1** was investigated. As shown in Fig. 2e, **1** exhibits a rapid wavelength-dependent response upon illumination with 400–700 nm light, without any apparent attenuation during the on/off switching cycles,

thereby indicating the efficient separation of photogenerated charge carriers.⁴³ The responsivity (R_λ), detectivity (D^*) and external quantum efficiency (EQE) at different wavelengths are summarized in **Supplementary Table 5**. Interestingly, the largest value of R_λ was achieved at 600 nm (Fig. 2f), which is inconsistent with the maximum absorption in UV-Vis spectrum (**Supplementary Fig. 19a**), thereby suggesting a temporary unclear process that enhanced the photocurrent at longer wavelengths.⁴³ Moreover, the R_λ and D^* values of **1** increased as the light intensity decreased (**Supplementary Fig. 20**). Thus, with its outstanding conductivity, fast turn-over response, and good reproducibility, **1** displays potential for use in optoelectrical applications.⁴³ In the context of **2**, the conductivity was determined to be only $1.89 \times 10^{-9} \text{ S cm}^{-1}$ at 25°C, with an E_a of 0.64 eV (**Supplementary Fig. 21**), while its photoconductivity performance was also significantly poorer than that of **1** (**Supplementary Fig. 22**). The enormous conductivity disparity between **1** and **2** was mainly attributed to their different structures and compositions. We speculated that the substitution of Cd with Cu in the 1D T2-CdGeSe chain may largely improve the intrinsic conductivity due to the superior conductivity of Cu compared to Cd. Combined with the narrow optical bandgap, a good oriented photoconductive behavior can be observed in **1**.

Theoretical DFT study of 1. To gain deep insight into the intrinsic electronic properties of **1**, density functional theory (DFT) calculations on the band structure and the projected density of states (PDOS) were performed, whereby **1** was found to exhibit a quasi-direct bandgap of 0.92 eV at the gamma point (left of Fig. 3a), consistent with the experimental value.

Compared with the almost flat band lines close to the valence band maximum (VBM) along the whole Brillouin zone, which are mainly dominated by the Cu d orbital and the Se p orbital (right of Fig. 3a **and Supplementary Fig. 23**), the bands near the conduction band minimum (CBM), which are contributed primarily by the Ge s orbital and the Se p orbital, along with negligible contributions from the Cu d orbital (right of Fig. 3a **and Supplementary Fig. 23**), show a significantly steep dispersion with an energy difference of ~ 0.71 eV (0.63 eV) along the $\Gamma \rightarrow A$ ($K \rightarrow H$ and $M \rightarrow L$) directions in reciprocal space, corresponding to the tubular direction (or c axis) in real space, while for other paths with high symmetry points, the dispersion widths are small (maximum energy difference < 0.1 eV). The relatively large dispersion strength of the energy bands indicates the facile transport of charge carriers along the c direction,^{38,44} which is of paramount importance to photoconductive devices. Moreover, the narrow band width and flat band lines near the VBM were attributed to the relatively larger localization of the Cu d orbital compared to the Ge s orbital. The other elements (K, O and H atoms) do not contribute to the electronic band edges. In addition, according to the charge density distributions of the VBM and the CBM (Fig. 3b-e), the CBM was determined to be mainly localized on the Se atoms and the Ge(2) and Ge(3) atoms, while Ge(1) atoms make no contribution. Therefore, combined with the above analysis and the features of the crystal structure, we deduced that the excellent conductivity of **1** may be attributed to the more facile oriented transport of electrons in the tubular direction (or along the c axis), in addition to obstructed carrier transport in the ab plane perpendicular to the tubular direction.

In summary, we report an unprecedented supertetrahedral chalcogenide cluster-based crystalline inorganic nanotube array, representing an important first step toward novel nanotube materials. The fine electrical conductivity, oriented photoconductive property, and well-defined structure of **1** render it a fascinating structural model in the optoelectronic and electronic fields. In addition, the precise potassium ions located around or within the nanotubes introduce a platform for the further study of ion transport. Finally, research exploring the syntheses of supertetrahedral chalcogenide cluster-based nanotubes with attractive functions and properties, such as ion-exchange and sensing, are currently underway, and the results will be presented in future work.

Methods

Synthesis of compound 1. Germanium dioxide (54 mg, 0.52 mmol), copper acetate hydrate (50 mg, 0.25 mmol), selenium powder (240 mg, 3.04 mmol), potassium sulfide (90 mg, 0.82 mmol), DBU (2.00 mL), (\pm)-2-amino-1-butanol (1.00 mL) and deionized water (1.00 mL) were mixed in a 25 mL Teflon-lining stainless steel and stirred for 30 min, then heated to 180 °C for 9 days. After cooling down to room temperature, a small amount of red rod crystals was obtained by sonication treatment in ethyl alcohol (yield: < 1%, based on Cu element).

Synthesis of compound 2. Germanium dioxide (104 mg, 0.99 mmol), cadmium acetate dihydrate (72 mg, 0.27 mmol), selenium powder (180 mg, 2.28 mmol), potassium sulfide (90 mg, 0.82 mmol), DBU (2.00 mL), (\pm)-2-amino-1-butanol (1.00 mL) and deionized water (1.00 mL) were mixed in a 25 mL Teflon-lining stainless steel and stirred for 30 min, then heated to 180 °C for 9 days. After cooling down to room temperature, a small amount of yellow rod crystals was obtained by sonication treatment in ethyl alcohol.

Electrical Conductivity Measurement. The temperature-dependent I-V curve measurements for the single crystal of compound **1** and **2** with a direct current two terminal method were on KEITHLEY4200-SCS with an oven. Each measurement was performed on several independent single crystals of compound **1** and **2**.

Photodetector Fabrication and Measurement. The metal chalcogenide-based photodetection device was fabricated by placing the single crystal between two gold electrodes glued by electrically conductive silver paste. For photodetection characterizations, the device was perpendicularly illuminated by monochromatic light with different wavelengths in vacuum. The photocurrent was recorded through semiconductor characterization system (4200-SCS, Keithley).

Details of the first-principle simulations. All Our calculations were carried out using density functional theory (DFT) as implemented in the VASP program. The interaction between the core and valence electrons for all atoms in the system was described using the projector augmented wave (PAW) approach. The generalized gradient approximation (GGA) of the Perdew-Burke-Ernzerhof (PBE) functional was used for the exchange correlation functional. Furthermore, in order to capture the weak van der Waals (VDW) interactions within this system, which was corrected by Grimme DFT-D2 method. Notably, the crystal structure required for the simulation here is obtained by experimental analysis using single-crystal

X-ray diffraction, and then detailed optimization of the atomic position based on the VASP software. The crystal structure was fully relaxed until total energies (atomic forces) converged to 10^{-4} eV (0.02 eV/Å) with the kinetic energy cutoff for plane-wave basis set to 400 eV. A $1 \times 1 \times 5$ Monkhorst-Pack k-point mesh has been used for structural optimization and a $2 \times 2 \times 10$ mesh has adopted for electronic structure calculation.

Declarations

Data availability

The X-ray crystallographic coordinates for **1** and **2** have been deposited at the Cambridge Crystallographic Data Centre (CCDC), under deposition numbers CCDC 2052331 and 2052336. These data can be obtained free of charge from The Cambridge Crystallographic Data Centre via www.ccdc.cam.ac.uk/data_request/cif. All remaining data are either providing in the Article and its supplementary information or are available from the authors upon reasonable request.

References

1. Iijima S. Helical microtubules of graphitic carbon. *Nature* **354**, 56-58 (1991).
2. Goldberger J, et al. Single-crystal gallium nitride nanotubes. *Nature* **422**, 599-602 (2003).
3. Otsubo K, et al. Bottom-up realization of a porous metal–organic nanotubular assembly. *Nat. Mater.* **10**, 291-295 (2011).
4. Murdock CR, Jenkins DM. Isostructural Synthesis of Porous Metal–Organic Nanotubes. *J. Am. Chem. Soc.* **136**, 10983-10988 (2014).
5. Liang R-R, A R-H, Xu S-Q, Qi Q-Y, Zhao X. Fabricating Organic Nanotubes through Selective Disassembly of Two-Dimensional Covalent Organic Frameworks. *J. Am. Chem. Soc.* **142**, 70-74 (2020).
6. Wang G-E, Xu G, Liu B-W, Wang M-S, Yao M-S, Guo G-C. Semiconductive Nanotube Array Constructed from Giant $[\text{Pb}^{\text{II}}_{18}\text{I}_{54}(\text{I}_2)^9]$ Wheel Clusters. *Angew. Chem. Int. Ed.* **55**, 514-518 (2016).
7. Chintakrinda K, et al. Atomically Precise Titanium-Oxo Nanotube with Selective Water Adsorption and Semiconductive Behaviors. *CCS Chemistry* **2**, 209-215 (2020).
8. Cao G-J, Liu J-D, Zhuang T-T, Cai X-H, Zheng S-T. A polyoxometalate–organic supramolecular nanotube with high chemical stability and proton-conducting properties. *Chem. Commun.* **51**, 2048-2051 (2015).
9. Zhou X, Liu N, Schmuki P. Photocatalysis with TiO_2 Nanotubes: “Colorful” Reactivity and Designing Site-Specific Photocatalytic Centers into TiO_2 Nanotubes. *ACS Catal.* **7**, 3210-3235 (2017).
10. Zhou Z, He C, Xiu J, Yang L, Duan C. Metal–Organic Polymers Containing Discrete Single-Walled Nanotube as a Heterogeneous Catalyst for the Cycloaddition of Carbon Dioxide to Epoxides. *J Am Chem Soc.* **137**, 15066-15069 (2015).

11. Jia J-G, Feng J-S, Huang X-D, Bao S-S, Zheng L-M. Homochiral iron(ii)-based metal–organic nanotubes: metamagnetism and selective nitric oxide adsorption in a confined channel. *Chem. Commun.* **55**, 2825-2828 (2019).
12. Jin B, Zhou X, Huang L, Lickleder M, Yang M, Schmuki P. Aligned MoO_x/MoS₂ Core–Shell Nanotubular Structures with a High Density of Reactive Sites Based on Self-Ordered Anodic Molybdenum Oxide Nanotubes. *Angew. Chem. Int. Ed.* **55**, 12252-12256 (2016).
13. Öner IH, et al. High Electromagnetic Field Enhancement of TiO₂ Nanotube Electrodes. *Angew. Chem. Int. Ed.* **57**, 7225-7229 (2018).
14. Katwal G, Paulose M, Rusakova IA, Martinez JE, Varghese OK. Rapid Growth of Zinc Oxide Nanotube–Nanowire Hybrid Architectures and Their Use in Breast Cancer-Related Volatile Organics Detection. *Nano Lett.* **16**, 3014-3021 (2016).
15. Xu J, Zhou X, Gao Z, Song Y-Y, Schmuki P. Visible-Light-Triggered Drug Release from TiO₂ Nanotube Arrays: A Controllable Antibacterial Platform. *Angew. Chem. Int. Ed.* **55**, 593-597 (2016).
16. Malliakas CD, Kanatzidis MG. Inorganic Single Wall Nanotubes of SbPS_{4-x}Se_x (0 ≤ x ≤ 3) with Tunable Band Gap. *J. Am. Chem. Soc.* **128**, 6538-6539 (2006).
17. Choudhury A, Dorhout PK. An Ordered Assembly of Filled Nanoscale Tubules of Europium Selenosilicate in the Crystal Structure of a Quaternary Compound. *J. Am. Chem. Soc.* **129**, 9270-9271 (2007).
18. Lin H, et al. Bulk assembly of organic metal halide nanotubes. *Chem. Sci.* **8**, 8400-8404 (2017).
19. Wu S, et al. Complex clover cross-sectioned nanotubules exist in the structure of the first uranium borate phosphate. *Chem. Commun.* **48**, 3479-3481 (2012).
20. Choudhury A, Grandjean F, Long GJ, Dorhout PK. Na_{1.515}EuGeS₄, A Three-Dimensional Crystalline Assembly of Empty Nanotubules Constructed with Europium(II/III) Mixed Valence Ions. *Inorganic Chemistry* **51**, 11779-11786 (2012).
21. Pan Q, et al. [Ni(1,2-PDA)₃]₂(HOCH₂CH₂CH₂NH₃)₃(H₃O)₂ [Ge₇O₁₄X₃]₃ (X = F, OH): A New 1D Germanate with 12-Ring Hexagonal Tubular Channels. *Chem. Mater.* **20**, 370-372 (2008).
22. Alekseev EV, Krivovichev SV, Depmeier W. A Crown Ether as Template for Microporous and Nanostructured Uranium Compounds. *Angew. Chem. Int. Ed.* **47**, 549-551 (2008).
23. Krivovichev SV, Kahlenberg V, Tananaev IG, Kaindl R, Mersdorf E, Myasoedov BF. Highly Porous Uranyl Selenate Nanotubules. *J. Am. Chem. Soc.* **127**, 1072-1073 (2005).
24. Krivovichev SV, Kahlenberg V, Kaindl R, Mersdorf E, Tananaev IG, Myasoedov BF. Nanoscale Tubules in Uranyl Selenates. *Angew. Chem. Int. Ed.* **44**, 1134-1136 (2005).
25. Millet P, Henry JY, Mila F, Galy J. Vanadium(IV)–Oxide Nanotubes: Crystal Structure of the Low-Dimensional Quantum Magnet Na₂V₃O₇. *J. Solid State Chem.* **147**, 676-678 (1999).
26. Lin Q, et al. High proton conductivity in metalloring-cluster based metal-organic nanotubes. *Nano Research* **14**, 387-391 (2021).

27. Yang D, et al. Selective electroreduction of carbon dioxide to methanol on copper selenide nanocatalysts. *Nat. Commun.* **10**, 677 (2019).
28. Zhang J, Bu X, Feng P, Wu T. Metal Chalcogenide Supertetrahedral Clusters: Synthetic Control over Assembly, Dispersibility, and Their Functional Applications. *Acc. Chem. Res.* **53**, 2261-2272 (2020).
29. Corrigan JF, Fuhr O, Fenske D. Metal Chalcogenide Clusters on the Border between Molecules and Materials. *Adv. Mater.* **21**, 1867-1871 (2009).
30. Feng P, Bu X, Zheng N. The Interface Chemistry between Chalcogenide Clusters and Open Framework Chalcogenides. *Acc. Chem. Res.* **38**, 293-303 (2005).
31. Philippot E, Ribes M, Lindqvist O. Crystal Structure of $\text{Na}_4\text{Ge}_4\text{S}_{10}$. *Rev. Chim. Miner.* **8**, 477-489 (1971).
32. Tan K, Ko Y, Parise JB, Darovsky A. Hydrothermal Growth of Single Crystals of TMA-CuGeS-2, $[\text{C}_4\text{H}_{12}\text{N}]_6[(\text{Cu}_{0.44}\text{Ge}_{0.56}\text{S}_{2.23})_4(\text{Ge}_4\text{S}_8)_3]$ and Their Characterization Using Synchrotron/Imaging Plate Data. *Chem. Mater.* **8**, 448-453 (1996).
33. Zhang J, Wang X, Lv J, Li D-S, Wu T. A multivalent mixed-metal strategy for single- Cu^+ -ion-bridged cluster-based chalcogenide open frameworks for sensitive nonenzymatic detection of glucose. *Chem. Commun.* **55**, 6357-6360 (2019).
34. Bowes CL, et al. Dimetal Linked Open Frameworks: $[(\text{CH}_3)_4\text{N}]_2(\text{Ag}_2, \text{Cu}_2)\text{Ge}_4\text{S}_{10}$. *Chem. Mater.* **8**, 2147-2152 (1996).
35. Tan K, Darovsky A, Parise JB. Synthesis of a novel open-framework sulfide, $\text{CuGe}_2\text{S}_5 \cdot (\text{C}_2\text{H}_5)_4\text{N}$, and its structure solution using synchrotron imaging plate data. *J. Am. Chem. Soc.* **117**, 7039-7040 (1995).
36. Yaghi OM, Sun Z, Richardson DA, Groy TL. Directed Transformation of Molecules to Solids: Synthesis of a Microporous Sulfide from Molecular Germanium Sulfide Cages. *J. Am. Chem. Soc.* **116**, 807-808 (1994).
37. Achak O, Pivan JY, Maunaye M, Louër M, Louër D. The ab initio structure determination of $[(\text{CH}_3)_4\text{N}]_2\text{Ge}_4\text{MnS}_{10}$ from X-ray powder diffraction data. *J. Alloys Compd.* **219**, 111-115 (1995).
38. Pathak A, et al. Integration of a $(-\text{Cu}-\text{S}-)_n$ plane in a metal-organic framework affords high electrical conductivity. *Nat. Commun.* **10**, 1721 (2019).
39. Yuan P, et al. Solvent-mediated assembly of atom-precise gold-silver nanoclusters to semiconducting one-dimensional materials. *Nat. Commun.* **11**, 2229 (2020).
40. Yang H, et al. The Largest Supertetrahedral Oxychalcogenide Nanocluster and Its Unique Assembly. *J. Am. Chem. Soc.* **140**, 11189-11192 (2018).
41. Li Y, et al. Coordination assembly of 2D ordered organic metal chalcogenides with widely tunable electronic band gaps. *Nat. Commun.* **11**, 261 (2020).
42. Chen T, et al. Continuous Electrical Conductivity Variation in $\text{M}_3(\text{Hexaiminotriphenylene})_2$ ($\text{M} = \text{Co}, \text{Ni}, \text{Cu}$) MOF Alloys. *J. Am. Chem. Soc.* **142**, 12367-12373 (2020).

43. Huang Q-Q, et al. Single-Component MLCT-Active Photodetecting Material Based on a Two-Dimensional Coordination Polymer. *CCS Chemistry* **2**, 655-662 (2020).
44. Jiang Y, et al. Synthesis of a Copper 1,3,5-Triamino-2,4,6-benzenetriol Metal–Organic Framework. *J. Am. Chem. Soc.* **142**, 18346-18354 (2020).

Figures

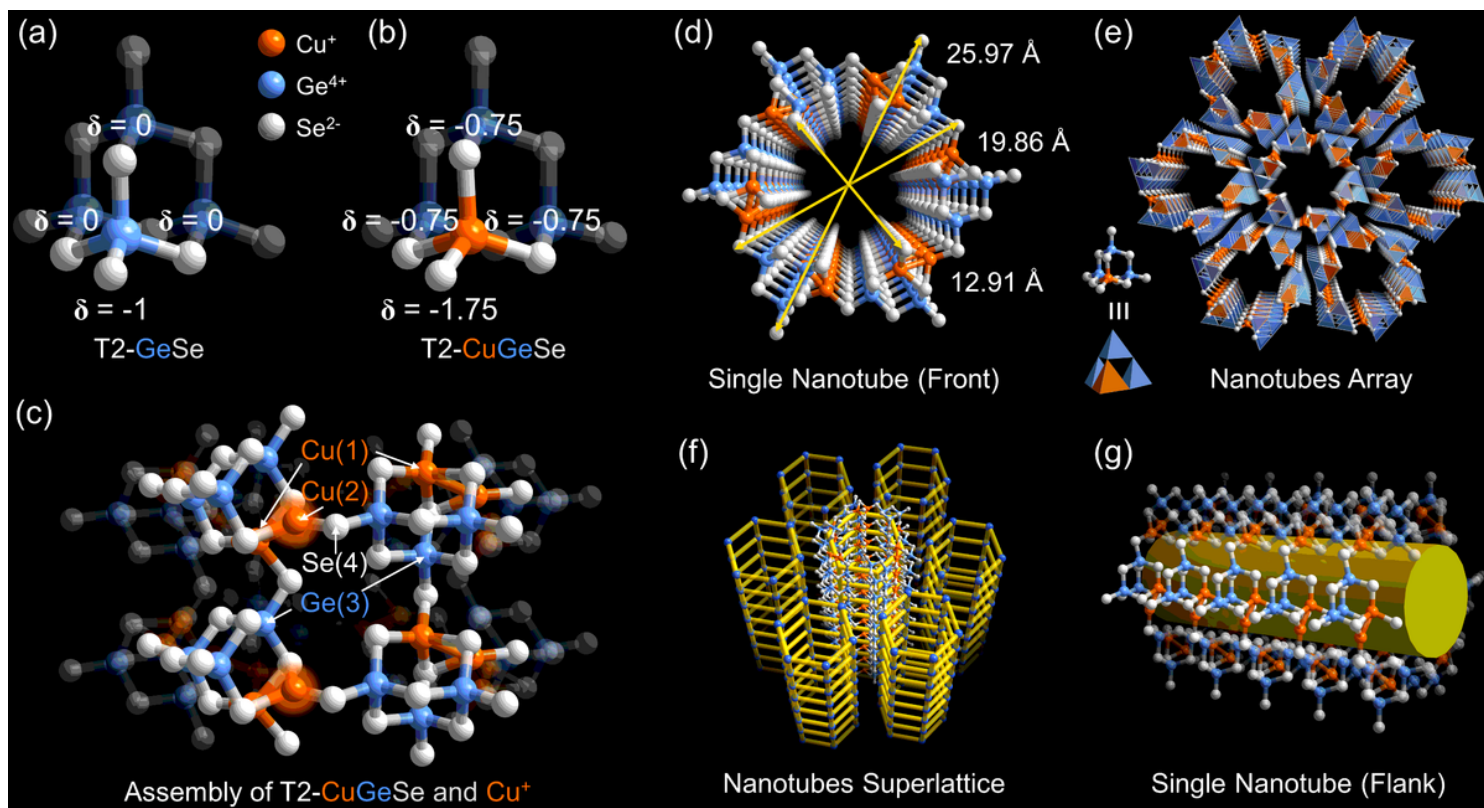


Figure 1

a Traditional homometallic supertetrahedral T2-GeSe cluster. b Heterometallic supertetrahedral T2-CuGeSe cluster (δ represents the theoretical residual charge of the Se atoms surrounding the corner Ge or Cu sites). c The connection mode of the T2-CuGeSe cluster in 1. d As-formed single 1D nanotube of 1 viewed along the c-axis. e Packing diagram of 1 viewed along the c-axis. f Pillared stacking of the connected wheel clusters in the axial direction. g Flank view of a single nanotube.

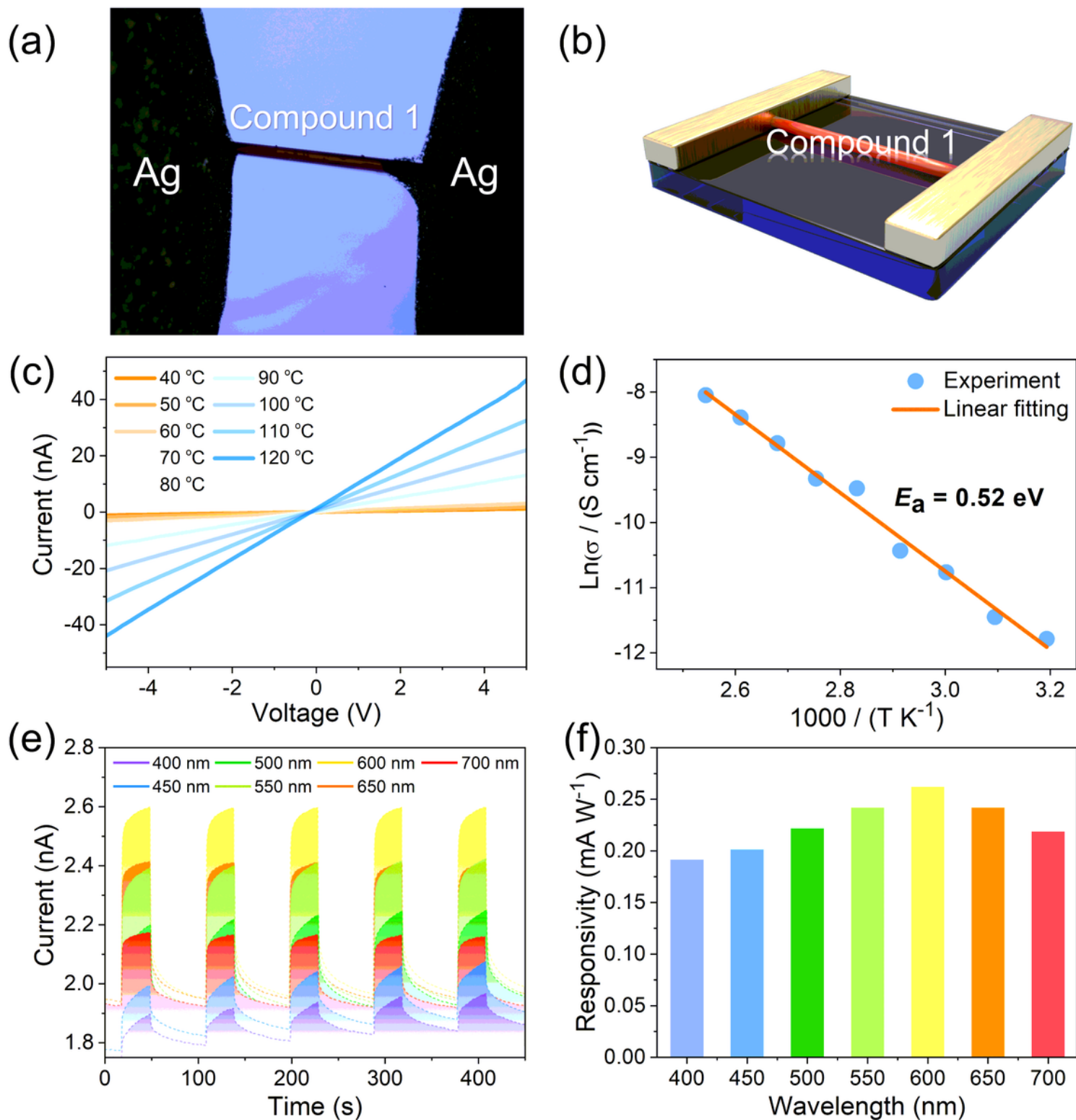


Figure 2

a Optical photographic image, and b schematic diagram of the single crystal of 1 used for electrical measurements. c Temperature-dependent I–V curves, and d corresponding Arrhenius plots for 1. e Time-dependent photocurrent response curves, and f responsivities of 1 under illumination at different light wavelengths.

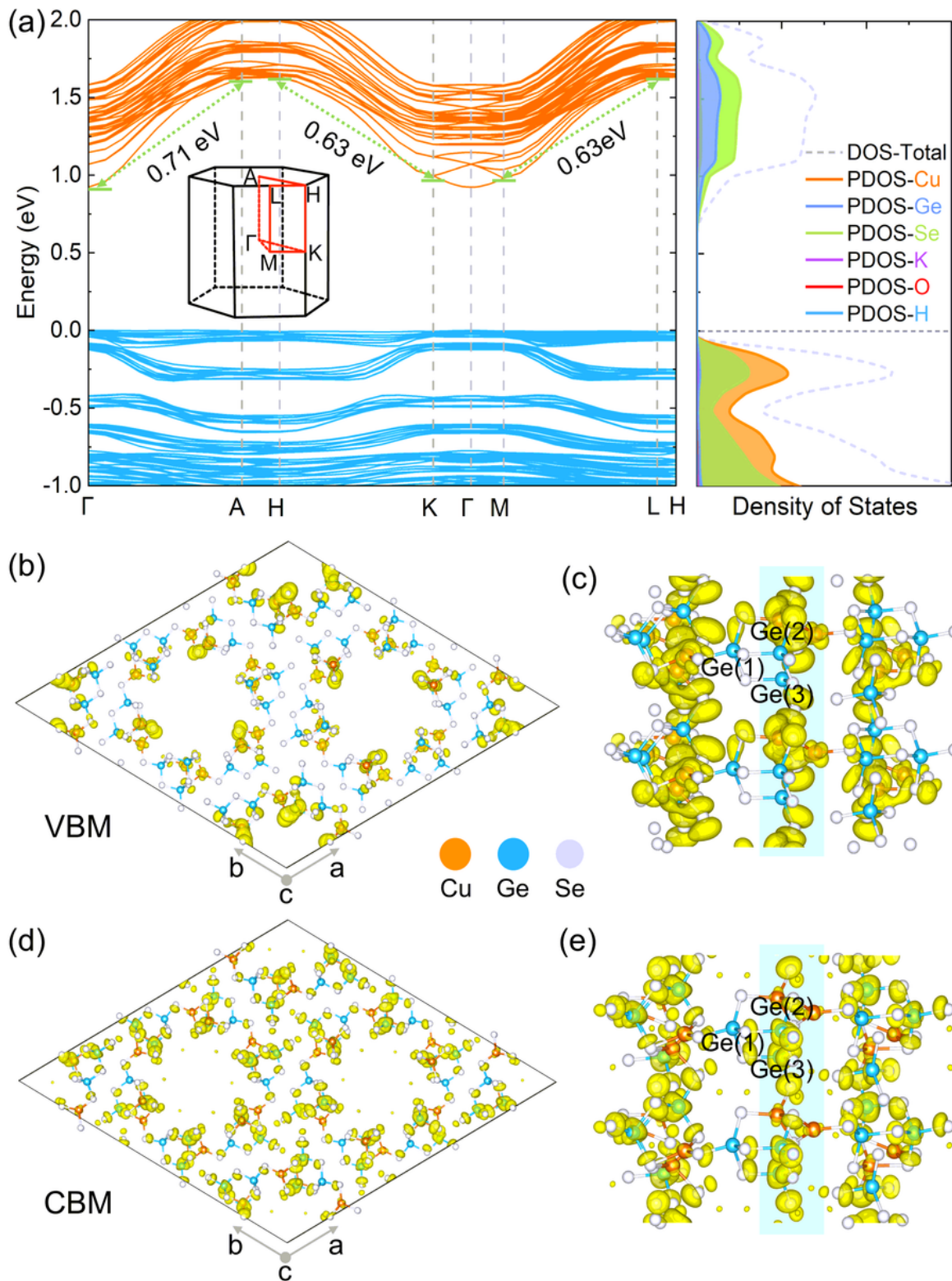


Figure 3

(a) Left panel, calculated band structure; Right panel, density of states (DOS) and projected DOS (PDOS) of 1, the gray dashed line at zero energy represents the Fermi level (E_F). (b, d) Front and (c, e) side views of the charge density iso-surfaces (yellow region) summed over the bands near the VBM and the CBM of 1. For the side views of the VBM and the CBM, a small fragment of a single nanotube is selected for

clarity. As the K, O, and H atoms do not contribute to the electronic band edges, they are omitted for clarity.

Supplementary Files

This is a list of supplementary files associated with this preprint. Click to download.

- [SupportingInformation.docx](#)
- [Scheme1.pdf](#)
- [Compound1.cif](#)
- [Compound2.cif](#)